

---

# Stateful ODE-Nets using Basis Function Expansions

---

**Alejandro Queiruga\***  
Google Research  
afq@google.com

**N. Benjamin Erichson\***  
University of Pittsburgh  
erichson@pitt.edu

**Liam Hodgkinson**  
ICSI and UC Berkeley  
liam.hodgkinson@berkeley.edu

**Michael W. Mahoney**  
ICSI and UC Berkeley  
mmahoney@stat.berkeley.edu

## Abstract

The recently-introduced class of ordinary differential equation networks (ODE-Nets) establishes a fruitful connection between deep learning and dynamical systems. In this work, we reconsider formulations of the weights as continuous-in-depth functions using linear combinations of basis functions which enables us to leverage parameter transformations such as function projections. In turn, this view allows us to formulate a novel stateful ODE-Block that handles stateful layers. The benefits of this new ODE-Block are twofold: first, it enables incorporating meaningful continuous-in-depth batch normalization layers to achieve state-of-the-art performance; second, it enables compressing the weights through a change of basis, without retraining, while maintaining near state-of-the-art performance and reducing both inference time and memory footprint. Performance is demonstrated by applying our stateful ODE-Block to (a) image classification tasks using convolutional units and (b) sentence-tagging tasks using transformer encoder units.

## 1 Introduction

The interpretation of neural networks (NNs) as discretizations of differential equations [7, 17, 31, 43] has recently unlocked a fruitful link between deep learning and dynamical systems. The strengths of so-called ordinary differential equation networks (ODE-Nets) are that they are well suited for modeling time series [11, 39] and smooth density estimation [14]. They are also able to learn representations that preserve the topology of the input space [9] (which may be seen as a “feature” or as a “bug”). Further, they can be designed to be highly memory efficient [13, 51]. However, one major drawback of current ODE-Nets is that the predictive accuracy for tasks such as image classification is often inferior as compared to other state-of-the-art NN architectures. The reason for the poor performance is two-fold: (a) ODE-Nets have shallow parameterizations (albeit long computational graphs), and (b) ODE-Nets do not include a mechanism for handling layers with internal state (i.e., stateful layers, or stateful modules), and thus cannot leverage batch normalization layers which are standard in image classification problems. That is, in modern deep learning environments the running mean and variance statistics of a batch normalization module are not trainable parameters, but are instead part of the module’s state, which does not fit into the ODE framework.

Further, traditional techniques such as stochastic depth [21], layer dropout [12] and adaptive depth [10, 28], which are useful for regularization and compressing traditional NNs, do not necessarily apply in a meaningful manner to ODE-Nets. That is, these methods do not provide a systematic scheme to derive smaller networks from a single deep ODE-Net source model. This limitation prohibits quick and rigorous adaptation of current ODE-Nets across different computational environments. Hence, there is a need for a general but effective way of reducing the number of parameters of deep ODE-Nets to reduce both inference time and the memory footprint.

To address these limitations, we propose a novel stateful ODE-Net model that is built upon the theoretical underpinnings of numerical analysis. Following recent work by [34, 37], we express the weights of an ODE-Net

---

\*Equal contributions.

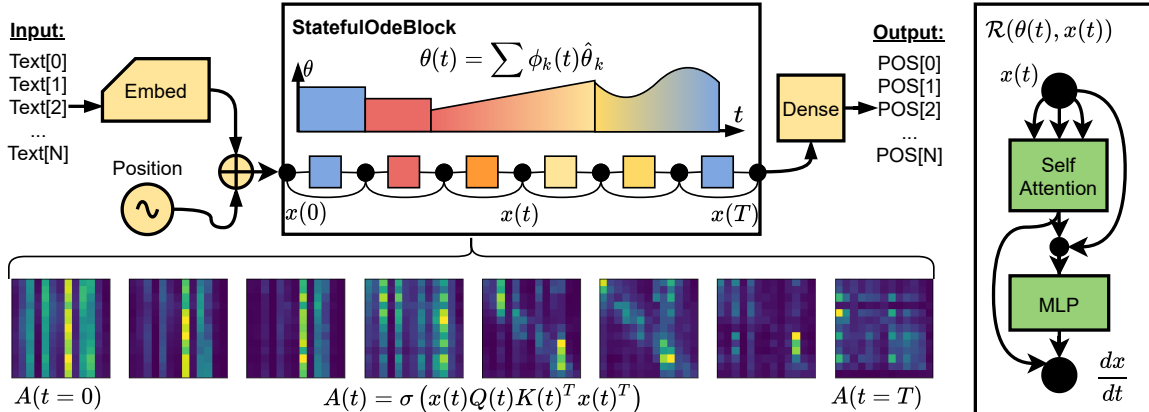


Figure 1: Sketch of a continuous-in-depth transformer-encoder. The model architecture consists of a sparse embedding layer followed by an OdeBlock that integrates the encoder to feed into a classification layer to determine parts of speech. The model graph is generated by nesting the residual  $\mathcal{R}$  on the right into a time-integration scheme in the OdeBlock. The weights for each call to  $\mathcal{R}$  are determined by evaluating the basis expansion. Internal hidden states evolve continuously during the forward pass. This is illustrated by a smoothly varying attention matrix.

as continuous-in-depth functions using linear combinations of basis functions. However, unlike prior works, we consider parameter transformations through a change of basis functions, i.e., *adding basis functions*, *decreasing the number of basis functions*, and *function projections*. In turn, we are able to (a) design deep ODE-Nets that leverage meaningful continuous-in-depth batch normalization layers to boost the predictive accuracy of ODE-Nets, e.g., we achieve 94.4% test accuracy on CIFAR-10, and 79.9% on CIFAR-100; and (b) we introduce a methodology for compressing ODE-Nets, e.g, we are able to reduce the number of parameters by a factor of two, *without retraining or revisiting data*, while nearly maintaining the accuracy of the source model.

In the following, we refer to our model as *Stateful ODE-Net*. Here are our main contributions.

- **Stateful ODE-Block.** We introduce a novel stateful ODE-Block that enables the integration of stateful network layers (Sec. 4.1). To do so, we view continuous-in-depth weight functions through the lens of basis function expansions and leverage basis transformations. An example is shown in Figure 1.
- **Stateful Normalization Layer.** We introduce stateful modules using function projections. This enables us to introduce continuous-in-depth batch normalization layers for ODE-Nets (Sec. 4.2). In our experiments, we show that such stateful normalization layers are crucial for ODE-Nets to achieve state-of-the-art performance on mainstream image classification problems (Sec. 7).
- **A Posteriori Compression Methodology.** We introduce a methodology to compress ODE-Nets without retraining or revisiting any data, based on parameter interpolation and projection (Sec. 5). That is, we can systematically derive smaller networks from a single deep ODE-Net source model through a change of basis. We demonstrate the accuracy and compression performance for various image classification tasks using both shallow and deep ODE-Nets (Sec. 7).
- **Advantages of Higher-order Integrators for Compression.** We examine the effects of training continuous-in-depth weight functions through their discretizations (Sec. 6). Our key insight in Theorem 1 is that higher-order integrators introduce additional implicit regularization which is crucial for obtaining good compression performance in practice. Proofs are provided in Appendix A.

## 2 Related Work

The “formulate in continuous time and then discretize” approach [7, 17] has recently attracted attention both in the machine learning and applied dynamical systems community. This approach considers a differential equation that defines the continuous evolution from an initial condition  $x(0) = x_{in}$  to the final output  $x(T) = x_{out}$  as

$$\dot{x}(t) = \mathcal{F}(\hat{\theta}, x(t), t). \quad (1)$$

Here, the function  $\mathcal{F}$  can be any NN that is parameterized by  $\hat{\theta}$ , with two inputs  $x$  and  $t$ . The parameter  $t \in [0, T]$  in this ODE represents time, analogous to the depth of classical network architectures. Using a finer temporal

Table 1: Comparison of our Stateful ODE-Net to other dynamical system inspired models.

Model	Multi-level	Compression	Basis Function View	Stateful Layers
NODE [7]	✗	✗	✗	✗
Multi-level ResNet [6]	✓	✗	✗	✗
Galerkin ODE-Net [34]	✗	✗	✓	✗
ContinuousNet [37]	✓	✗	✓	✗
Stateful ODE-Net (ours)	✓	✓	✓	✓

discretization (with a smaller  $\Delta t$ ) or a larger terminal time  $T$ , corresponds to deeper network architectures. Feed-forward evaluation of the network is performed by numerically integrating Eq. (1):

$$x_{out} = x_{in} + \int_0^T \mathcal{F}(\hat{\theta}, x(t), t) dt = \text{odeBlock} \left[ \mathcal{F}, \hat{\theta}, \text{scheme}, \Delta t, t \in [0, T] \right] (x_{in}). \quad (2)$$

Inspired by this view, numerous ODE and PDE-based network architectures [1, 8, 9, 15, 32, 42, 48, 49], and continuous-time recurrent units [4, 29, 30, 40, 41] have been proposed.

Recently, the idea of representing a continuous-time weight function as a linear combination of basis functions has been proposed by [34] and [37]. This involves using the following formulation:

$$\dot{x}(t) = \mathcal{R}(\theta(t; \hat{\theta}), x(t)), \quad (3)$$

where  $\mathcal{R}$  is now parameterized by a continuously-varying weight function  $\theta(t; \hat{\theta})$ . In turn, this weight function is parameterized by a countable tensor of trainable parameters  $\hat{\theta}$ . Both of these works noted that piecewise constant basis functions algebraically resemble residual networks and stacked ODE-Nets. A similar concept was used by [6] to inspire a multi-level refinement training scheme for discrete ResNets. In addition, [34] uses orthogonal basis sets to formulate a Gal erkin Neural ODE.

In this work, we take advantage of basis transformations to introduce stateful normalization layers as well as a methodology for compressing ODE-Nets, thus improving on ContinuousNet and other prior work [37]. Although basis elements are often chosen to be orthogonal, inspired by multi-level refinement training, we shall consider non-orthogonal basis sets in our experiments. Table 1 highlights the advantages of our model compared to other related models.

### 3 Basis Function View of Continuous-in-depth Weight Functions

Let  $\theta(t; \hat{\theta})$  be an arbitrary weight function that depends on depth (or time)  $t$ , which takes as argument a vector of real-valued weights  $\hat{\theta}$ . Given a basis  $\phi$ , we can represent  $\theta$  as a linear combination of  $K$  (continuous-time) basis functions  $\phi_k(t)$ :

$$\theta(t; \hat{\theta}) = \sum_{k=1}^K \phi_k(t) \hat{\theta}_k. \quad (4)$$

The basis sets which we consider have two parameters that specify the family of functions  $\phi$  and cardinality  $K$  (i.e., the number of functions) to be used. Hence, we represent a basis set by  $(\phi, K)$ . While our methodology can be applied to any basis set, we restrict our attention to piecewise constant and piecewise linear basis functions, common in finite volume and finite element methods [44, §4].

- **Piecewise constant basis.** This orthogonal basis consist of basis functions that assume a constant value for each of the elements of width  $\Delta t = T/K$ , where  $T$  is the ‘‘time’’ at the end of the ODE-Net. The summation in Eq. (4) involves piecewise-constant indicator functions  $\phi_k(t)$  satisfying

$$\phi_k(t) = \begin{cases} 1, & t \in [(k-1)\Delta t, k\Delta t] \\ 0, & \text{otherwise.} \end{cases} \quad (5)$$

- **Piecewise linear basis functions.** This basis consists of evenly spaced elements where each parameter  $\hat{\theta}_k$  corresponds to the value of  $\theta(t_k)$  at element boundaries  $t_k = T(k-1)/(K-1)$ . Each basis function is a ‘‘hat’’ function around the point  $t_k$ ,

$$\phi_k(t) = \begin{cases} (t - k\Delta t)/\Delta t, & t \in [(k-1)\Delta t, k\Delta t] \\ 1 - (t - k\Delta t)/\Delta t, & t \in [k\Delta t, (k+1)\Delta t] \\ 0, & \text{otherwise.} \end{cases} \quad (6)$$

Piecewise linear basis functions have compact and overlapping supports; i.e., they are not orthogonal, unlike piecewise constant basis functions.

### 3.1 Basis Transformations

We consider two avenues of basis transformation to change function representation: interpolation and projection. Note that these transformations will often introduce approximation error, particularly when transforming to a basis with a smaller size. Furthermore, interpolation and projection do not necessarily give the same result for the same function.

**Interpolation.** Some basis functions use control points for which parameters correspond to values at different  $t_k$  such that  $\theta(t_k, \hat{\theta}) = \hat{\theta}_k$ . Given  $\theta^1$ , the parameter coefficients for  $\theta^2$  can thus be calculated by evaluating the  $\theta^1$  at the control points  $t_k^2$ :

$$\hat{\theta}_k^2 = \theta^1(t_k^2, \hat{\theta}^1) = \sum_{b=1}^{K_1} \phi_b^1(t_k^2) \hat{\theta}_b^1 \quad \text{for } k = 1, \dots, K_2. \quad (7)$$

Interpolation only works with basis functions where the parameters correspond to control point locations. For piecewise constant basis functions,  $t_k$  corresponds to the cell centers, and for piecewise linear basis functions,  $t_k$  corresponds to the endpoints at element boundaries.

**Projection.** Function projection can be used with any basis expansion. Given the function  $\theta^1(t)$ , the coefficients  $\hat{\theta}_k^2$  are solved by a minimization problem:

$$\min_{\hat{\theta}_k^2} \int_0^T \left( \theta^1(t, \hat{\theta}^1) - \theta^2(t, \hat{\theta}^2) \right)^2 dt = \min_{\hat{\theta}_k^2} \int_0^T \left( \sum_{a=1}^{K_1} \hat{\theta}_a^1 \phi_a^1(t) - \sum_{k=1}^{K_2} \hat{\theta}_k^2 \phi_k^2(t) \right)^2 dt. \quad (8)$$

Appendix C.1 includes the details of the numerical approximation of the loss and its solution. The integral is evaluated using Gaussian quadrature over sub-cells. The overall calculation solves the same linear problem repeatedly for each coordinate of  $\theta$  used by the call to  $\mathcal{R}$ .

## 4 Stateful ODE-Nets

Modern neural network architectures leverage stateful modules such as BatchNorms [22] to achieve state-of-the-art performance, and recent work has demonstrated that ODE-Nets also can benefit from normalization layers [16]. However, incorporating normalization layers into ODE-Nets is challenging; indeed, recent work [45] acknowledges that it was not obvious how to include BatchNorm layers in ODE-Nets. The reason for this challenge is that normalization layers have internal state parameters with specific update rules, in addition to trainable parameters.

### 4.1 Stateful ODE-Block

To formulate a stateful ODE-Block, we consider the following differential equation:

$$\dot{x}(t) = \mathcal{R}(\theta^g(t), \theta^s(t), x(t)), \quad (9)$$

which is parameterized by two continuous-in-depth weight functions  $\theta^g(t, \hat{\theta}^g)$  and  $\theta^s(t, \hat{\theta}^s)$ , respectively. For example, the continuous-in-depth BatchNorm function has two gradient-parameter functions in  $\theta^g(t)$  – scale  $s(t)$  and bias  $b(t)$  – and two state-parameter functions in  $\theta^s(t)$  – mean  $\mu(t)$  and variance  $\sigma(t)$ . Using a functional programming paradigm inspired by Flax [20], we replace the internal state update of the module with a secondary output. The continuous update function  $\mathcal{R}$  is split into two components: the forward-pass output  $\dot{x} = \mathcal{R}_x$  and the state update output  $\theta^{s*} = \mathcal{R}_s$ . Then, we solve  $\dot{x}$  using methods for numerical integration (denoted by `scheme`), followed by a basis projection of  $\theta^{s*}$ . We obtain the following input-output relation for the forward pass during training:

$$\begin{cases} x_{out} &= \text{StatefulOdeBlock}_x[\mathcal{R}_x, \text{scheme}, \Delta t, \phi](\hat{\theta}^g, \hat{\theta}^s, x_{in}) \\ \hat{\theta}^{s*} &= \text{StatefulOdeBlock}_s[\mathcal{R}_s, \text{scheme}, \Delta t, \phi](\hat{\theta}^g, \hat{\theta}^s, x_{in}), \end{cases} \quad (10)$$

which we jointly optimize for  $\theta^g(t)$  and  $\theta^s(t)$  during training. Optimizing for  $\theta^g$  and  $\theta^s$  involves two coupled equations, updating the gradient with respect to the loss  $L$  and a fixed-point iteration on  $\theta^s$ ,

$$\theta^{g*}(t) = \theta^g(t) - \frac{\partial L}{\partial \theta^g(t)}(\theta^g(t), \theta^s(t), x_0), \quad (11)$$

$$\theta^{s*}(t) = \mathcal{R}_s(\theta^g(t), \theta^s(t), x(t)). \quad (12)$$

The updates to  $\theta^g(t)$  are computed by backpropagation of the loss through the ODE-Block with respect to its basis coefficients  $\frac{\partial x_{out}}{\partial \theta^g}$ . Optimizing  $\hat{\theta}^s(t)$  involves projecting the update rule back onto the basis during every training step.

## 4.2 Numerical Solution of Stateful Normalization Layers

While Eq. (12) can be computed given a forward pass solution  $x(t)$ , this naive approach requires implementing an additional numerical discretization. Instead, consider that each call to  $\mathcal{R}$  at times  $t_i \in [0, T]$  during the forward pass outputs an updated state  $\bar{\theta}_i^s = \mathcal{R}_s(t_i)$ . This generates a point cloud  $\{t_i, \bar{\theta}_i^s\}$  which can be projected back onto the basis set by minimizing the point-wise least-squared-error

$$\hat{\theta}^{s*} = \arg \min_{\hat{\theta}^{s*}} \sum_{i=1}^{N_{state}} \left( \bar{\theta}_i^s - \sum_{k=1}^K \phi_k(t_i) \hat{\theta}_k^{s*} \right)^2. \quad (13)$$

Algorithm 1 in the appendix describes the calculation of Eq. (10), fused into one loop. When using forward Euler integration and piecewise constant basis functions, this algorithm reduces to the forward pass and update rule in a ResNet with BatchNorm layers. This theoretical formalism and algorithm generalizes to any combination of stateful layer, basis set, and integration scheme.

## 5 A Posteriori Compression Methodology

Basis transformations of continuous functions are a natural choice for compressing ODE-Nets because they couple well with continuous-time operations. Interpolation and projection can be applied to the coefficients  $\hat{\theta}^g$  and  $\hat{\theta}^s$  to change the number of parameters needed to represent the continuous functions. Given the coefficients  $\hat{\theta}^1$  to a function  $\theta^1(t)$  on a basis  $(\phi^1, K_1)$ , we can determine new coefficients  $\hat{\theta}^2$  on a different space  $(\phi^2, K_2)$ . Changing the basis size can reduce the total number of parameters (to  $K_2 < K_1$ ), and hence the total storage requirement. This representation enables compression in a systematic way — in particular, we can consider a change of basis to transform learned parameter coefficients  $\hat{\theta}^1$  to other coefficients  $\hat{\theta}^2$ . To illustrate this, Figure 2 shows different basis representations of a weight function.

Note that this compression methodology also applies to basis function ODE-Nets that are trained without stateful normalization layers. Further, continuous-time formulations can also decrease the number of model steps, increasing inference speed, in addition to decreasing the model size.

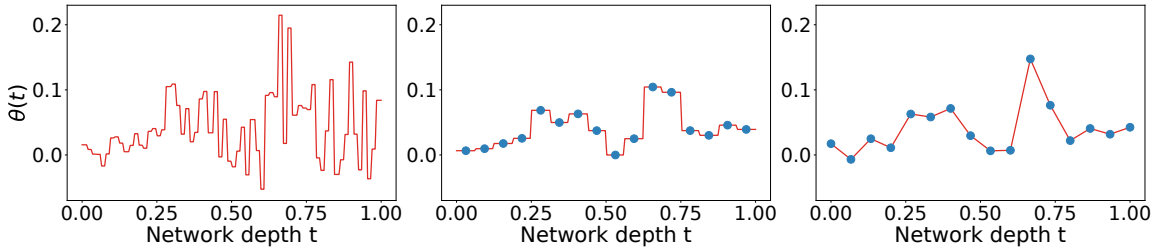


Figure 2: Example of projecting a component of the query kernel from a continuous-in-depth transformer. The model was trained with  $K = 64$  piecewise constant basis functions (left) and then projected to:  $K = 16$  piecewise constant basis functions (middle), and  $K = 16$  piecewise linear basis functions (left). Circles denote the control points (knots) corresponding to parameters  $\hat{\theta}_k$ .

## 6 Advantages of Higher-order Integrators for Compression

To implement any ODE-Net, it is necessary to approximately solve the corresponding ODE using a numerical integrator. There are many possible integrators one can use, so to take full advantage of our proposed methodology, we examine the advantages of certain integrators on compression from a theoretical point of view. In short, for the same step size, higher-order integrators exhibit increasing numerical instability if the underlying solution changes too rapidly. Because these large errors will propagate through the loss function, minimizing any loss computed on the numerically integrated ODE-Net will avoid choices of the weights that result in rapid dynamics. This is beneficial for compression, as slower, smoother dynamics in the ODE allow for coarser approximations in  $\theta$ .

To quantify this effect, we derive an asymptotic global error term for small step sizes. Our analysis focuses on *explicit Runge–Kutta (RK) methods*, although similar treatments are possible for most other integrators. For brevity, here we use  $h$  to denote step size in place of  $\Delta t$ . A  $p$ -stage explicit RK method for an ODE  $\dot{y}_\theta(t) = f(y_\theta(t), \theta(t))$  provides an approximation  $y_{h,\theta}(t)$  of  $y_\theta(t)$  for a given step size  $h$  on a discrete grid of points  $\{0, h, 2h, \dots\}$  (which can then be joined together through linear interpolation). As the order  $p$  increases, the error in the RK approximation generally decreases more rapidly in the step size for smooth integrands. However, a tradeoff arises through an increased sensitivity to any irregularities. We consider these properties from the perspective of *implicit regularization*, where the choice of integrator impacts the trained parameters  $\theta$ .

Implicit regularization is of interest in machine learning very generally [33], and in recent years it has received attention for NNs [25, 35]. In a typical theory-centric approach to describing implicit regularization, one derives an approximately equivalent *explicit regularizer*, relative to a more familiar loss function. In Theorem 1, we demonstrate that for any scalar loss function  $L$ , using a RK integrator *implicitly regularizes* towards smaller derivatives in  $f$ . Since  $\theta$  can be arbitrary, we consider finite differences in time. To this effect, recall that the  $m$ -th order forward differences are defined by  $\Delta_h^m f(x, t) = \Delta_h^{m-1} f(x, t+h) - \Delta_h^{m-1} f(x, t)$ , with  $\Delta_h^0 f(x, t) = f(x, t)$ . Also, for any  $t \in [0, T]$ , we let  $\iota_h(t) = \lfloor t/h \rfloor \cdot h$  denote the nearest point on the grid  $\{0, h, 2h, \dots\}$  to  $t$ .

**Theorem 1 (Implicit regularization)** *There exists a polynomial  $P$  depending only on the Runge-Kutta scheme satisfying  $P(0) = 0$ , and a smooth function  $\bar{y}_\theta(t)$  depending on  $f, \theta$ , and the scheme, such that for any  $t \in [0, T]$ , as  $h \rightarrow 0^+$ ,*

$$L(y_{h,\theta}(t)) = L(\bar{y}_\theta(t)) + h^p \nabla L(\bar{y}_\theta(t)) \cdot e_{h,\theta}(t) + \mathcal{O}(h^{p+1}), \quad (14)$$

where  $\dot{e}_{h,\theta}(t) = \frac{\partial f}{\partial y}(y_{h,\theta}(t), \theta(\iota_h(t)))e_{h,\theta}(t) + P \circ \mathcal{D}_{h,\theta}^p(t)$  and

$$\mathcal{D}_{h,\theta}^p(t) = \left\{ h^{-m} \Delta_h^m \frac{\partial^l f_j}{\partial y^l} f_j(y_{h,\theta}(t), \theta(\iota_h(t))) \right\}_{j=1, \dots, d, l+m \leq p+1}. \quad (15)$$

The proof is provided in Appendix A. Theorem 1 demonstrates that Runge-Kutta integrators implicitly regularize toward smaller derivatives/finite differences of  $f$  of orders  $k \leq p+1$ . To demonstrate the effect this has on compression, we consider the *sensitivity* of the solution  $y$  to  $\theta(t)$ , and hence to the choice of basis functions, using Gateaux derivatives. A smaller sensitivity to  $\theta(t)$  allows for coarser approximations before encountering a significant reduction in accuracy. The sensitivity of the solution in  $\theta(t)$  is contained in the following lemma.

**Lemma 1** *There exists a smooth function  $\bar{\theta}$  depending only on  $\theta$  such that for any smooth function  $\varphi(t)$ ,*

$$D_\varphi y_{h,\theta}(t) := \left. \frac{d}{d\epsilon} y_{h,\theta+\epsilon\varphi}(t) \right|_{\epsilon=0} = \int_0^t e^{F_{h,\theta}(s,t)} \frac{\partial f}{\partial \theta}(y_{h,\theta}(s), \bar{\theta}(s)) \varphi(s) ds + \mathcal{O}(h^p),$$

where  $F_{h,\theta}(s, t) = \int_s^t \frac{\partial f}{\partial y}(y_{h,\theta}(u), \bar{\theta}(u)) du$ .

Simply put, Lemma 1 shows that the sensitivity of  $y_{h,\theta}(t)$  in  $\theta$  decreases monotonically with decreasing derivatives of the integrand  $f$  in each of its arguments. These are precisely the objects that appear in Theorem 1. Therefore, a reduced sensitivity can occur in one of two ways:

- (I) A higher-order integrator is used, causing higher-order derivatives to appear in the implicit regularization term  $e_{h,\theta}$ . By the Landau-Kolmogorov inequality [26], for any differential  $D$  and integer  $m \geq 1$ ,  $\|D^m f\| \geq c_m \|f\| (\|Df\|/\|f\|)^m$  for some  $c_m > 0$ . Hence, by implicitly regularizing towards smaller higher-order derivatives/finite differences, we should expect more dramatic reductions in the first-order derivative/finite difference as well.

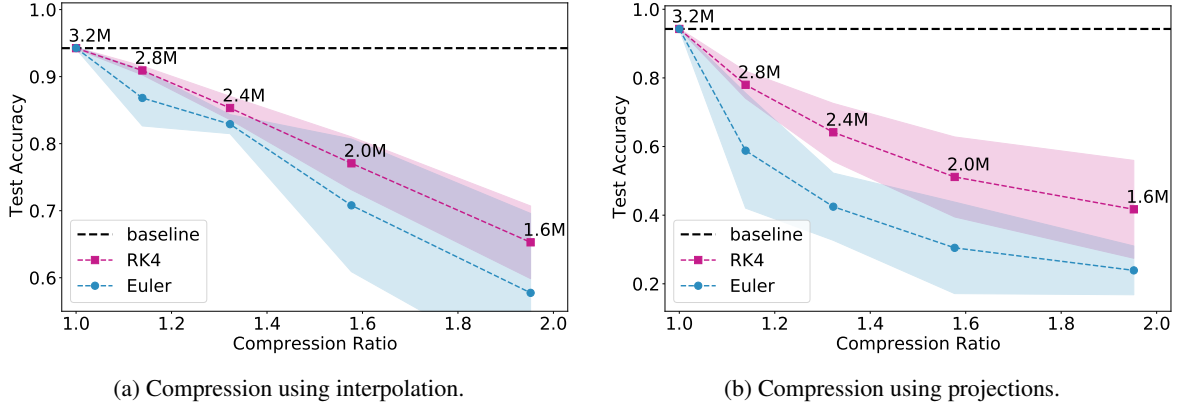


Figure 3: Higher-order integrators introduce additional implicit regularization into learned continuous weight functions. By experimenting on CIFAR-10, it is empirically observed that training with the RK4 scheme improves the compression-performance compared to using the forward Euler scheme.

(II) A larger step size  $h$  is used. Since doing so can lead to stability concerns during training, we later consider a refinement training scheme [6, 37] where  $h$  is slowly reduced.

In Figure 3, we verify strategy (I), showing that the 4th-order RK4 scheme exhibits improved test accuracy for higher compression ratios over the 1st-order Euler scheme. Unfortunately, higher-order integrators typically increase the runtime on the order of  $\mathcal{O}(p)$ . Therefore, some of our later experiments will focus on strategy (II), which avoids this issue.

## 7 Empirical results

We present empirical results to demonstrate the predictive accuracy and compression performance of Stateful ODE-Nets for both image classification and NLP tasks. Each experiment was repeated with eight different seeds, and the figures report mean and standard deviations. Details about the training process, and different model configurations are provided in Appendix E. Research code is provided as part of the following GitHub repository: <https://github.com/afqueiruga/StatefulOdeNets>. Our models are implemented in Jax [3], using Flax [20].

### 7.1 Compressing Shallow ODE-Nets for Image Classification Tasks

First, we consider shallow ODE-Nets, which have low parameter counts, in order to compare our models to meaningful baselines from the literature. We evaluate the performance on both MNIST [27] and CIFAR-10 [24]. Here, we train our Stateful ODE-Net using the classic Runge-Kutta (RK4) scheme and the multi-level refinement method proposed by [6, 37].

**Results for MNIST.** Due to the simplicity of this problem, we consider for this experiment a model that has only a single OdeBlock with 8 units, and each unit has 12 channels. Our model has about  $18K$  parameters and achieves about 99.4% test accuracy on average. Despite the lower parameter count, we outperform all other ODE-based networks on this task, as shown in Table 2. We also show an ablation model by training our ODE-Net without continuous-in-depth batch normalization layers while keeping everything else fixed. The ablation experiment shows that normalization provides only a slight accuracy improvements; this is to be expected as MNIST is a relatively easy problem.

Next, we compress our model by reducing the number of basis functions and timesteps from 8 down to 4. We do this without retraining, fine-tuning, or revisiting any data. The resulting model has approximately  $10K$  parameters (a 45% reduction), while achieving about 99.2% test accuracy. We can compress the model even further to  $7K$  parameters, if we are willing to accept a 2.6% drop in accuracy. Despite this drop, we still outperform a simple NODE model with  $84K$  parameters. Further, we can see that the inference time (evaluated over the whole test set) is significantly reduced.

**Results for CIFAR-10.** Next, we demonstrate the compression performance on CIFAR-10. To establish a baseline that is comparable to other ODE-Nets, we consider a model that has two OdeBlocks with 8 units, and the units

Table 2: Compression performance and test accuracy of shallow ODE-Nets on MNIST.

Model	Best	Average	Min	# Parameters	Compression	Inference
NODE [9]	-	96.4%	-	84K	-	-
ANODE [9]	-	98.2%	-	84K	-	-
2nd-Order [34]	-	99.2%	-	20K	-	-
A4+NODE+NDDE [50]	-	98.5%	-	84K	-	-
Ablation Model	99.3%	99.1%	98.9%	18K	-	-
Stateful ODE-Net (ours)	<b>99.6%</b>	<b>99.4%</b>	<b>99.3%</b>	18K	baseline	1.7 (s)
↔ (compressed)	99.4%	99.2%	99.1%	10K	45%	1.2 (s)
↔ (compressed)	97.8%	96.9%	95.7%	7K	61%	1.1 (s)

Table 3: Compression performance and test accuracy of shallow ODE-Nets on CIFAR-10.

Model	Best	Average	Min	# Parameters	Compression	Inference
HyperODENet [45]	-	87.9%	-	460K	-	-
SDE BNN (+ STL) [45]	-	89.1%	-	460K	-	-
Hamiltonian [42]	-	89.3%	-	264K	-	-
NODE [9]	-	53.7%	-	172K	-	-
ANODE [9]	-	60.6%	-	172K	-	-
A4+NODE+NDDE [50]	-	59.9%	-	107K	-	-
Ablation Model	88.9%	88.4%	88.1%	204K	-	-
Stateful ODE-Net (ours)	<b>90.7%</b>	<b>90.4%</b>	<b>90.1%</b>	207K	baseline	2.1 (s)
↔ (compressed)	90.3%	89.9%	89.6%	114K	45%	1.6 (s)

in the first block have 16 channels, while the units in the second block have 32 channels. Our model has about 207K parameters and achieves about 90.4% accuracy. Note, that our model has a similar test accuracy to that of a ResNet-20 with 270K parameters (a ResNet-20 yields about 91.25% accuracy [19]). In Table 3 we see that our model outperforms all other ODE-Nets on average, while having a comparable parameter count. The ablation model is not able to achieve state-of-the-art performance here, indicating the importance of normalization layers.

As before, we compress our model by reducing the number of basis functions and timesteps from 8 down to 4. The resulting model has 114K parameters and achieves about 89.9% accuracy. Despite the compression ratio of nearly 2, the performance of our compressed model is still better as compared to other ODE-Nets. Again, it can be seen that the inference time on the test set is greatly reduced.

## 7.2 Compressing Deep ODE-Nets for Image Classification Tasks

Next, we demonstrate that we can also compress high-capacity deep ODE-Nets trained on CIFAR-10. We consider a model that has 3 stateful ODE-blocks. The units within the 3 blocks have an increasing number of channels: 16,32,64. Additional results for CIFAR-100 are provided in Appendix D.

Table 4 shows results for CIFAR-10. Here we consider two configurations: (c1) is a model trained with refinement training, which has piecewise linear basis functions; (c2) is a model trained without refinement training, which has piecewise constant basis functions. It can be seen that model (c2) achieves high predictive accuracy, yet it yields a poor compression performance. In contrast, model (c1) is about 1.5% less accurate, but it shows to be highly compressible. We can compress the parameters by nearly a factor of 2, while increasing the test error only by 0.6%. Further, the ablation model shows that normalization layers are crucial for training deep ODE-Nets on challenging problems. Here, the ablation model that is trained without our continuous-in-depth batch normalization layers does not converge and achieves a performance similar to tossing a 10-sided dice.

In Figure 4a, we show that the compression performance of model (c1) depends on the particular choice of basis set that is used during training and inference time. Using piecewise constant basis functions during training yields models that are slightly less compressible (green line), as compared to models that are using piecewise linear basis functions (blue line). Interestingly, the performance can be even further improved by projecting the piecewise linear basis functions onto piecewise constant basis functions during inference time (red line). In Figure 4b, we show that we can also decrease the number of time steps  $N_T$  during inference time, which in turn leads to a



Table 4: Compression performance and test accuracy of deep ODE-Nets on CIFAR-10.

Model	Best	Average	Min	# Parameters	Compression	Inference
ResNet-110 [19]	-	93.4%	-	1.73M	-	-
ResNet-122-i [6]	-	93.8%	-	1.92M	-	-
MidPoint-62 [5]	-	92.8%	-	1.78M	-	-
ContinuousNet [37]	94.0%	93.8%	93.5%	3.19M	-	-
Ablation Model	10.0%	10.0%	10.0%	1.62K	-	-
Stateful ODE-Net (c1)	93.0%	92.4%	92.1%	1.63M	baseline	3.4 (s)
↪ (compressed)	92.2%	91.8%	91.1%	0.85M	48%	2.3 (s)
Stateful ODE-Net (c2)	<b>94.4%</b>	<b>94.1%</b>	<b>93.8%</b>	1.63M	baseline	3.4 (s)
↪ (compressed)	69.9%	60.5%	52.7%	0.85M	48%	2.3 (s)

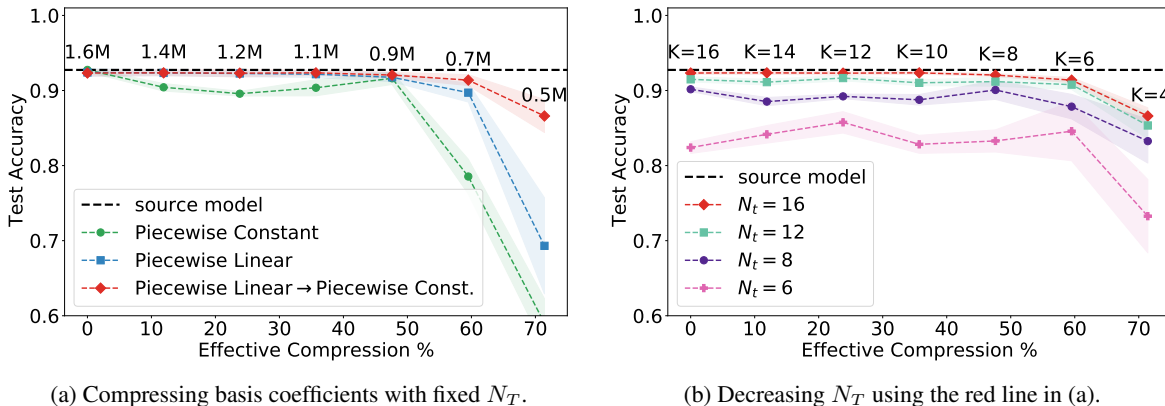


Figure 4: In (a) we show the prediction accuracy on CIFAR-10 as a function of weight compression for models that are trained with different basis functions. It can be seen that there is advantage of using piecewise linear basis functions during training. In (b) we compare models with different numbers of time steps. Reducing the number of time-steps reduces the the number of FLOPs.

reduction of the number of FLOPs during inference time. Recall,  $N_T$  refers to the number of time steps, which in turn determines the depth of the model graph. For instance, reducing  $N_T$  from 16 to 8, reduces the inference time by about a factor of 2, while nearly maintaining the predictive accuracy.

### 7.3 Compressing Continuous Transformers

A discrete transformer-based encoder can be written as

$$x_{t+1} = x_t + T(q, x_t) + M(\rho, x_t + T(q, x_t)) \quad (16)$$

where  $T(q, x)$  is self attention (SA) with parameters  $q$  (appearing twice due to the internal skip connection) and  $M$  is a multi-layer perceptron (MLP) with parameters  $\rho$ . Repeated transformer-based encoder blocks can be phrased as an ODE with the equation

$$\dot{x} = T(q(t), x) + M(\rho(t), x + T(q(t), x)). \quad (17)$$

Recognizing  $\theta(t) = \{q(t), \rho(t)\}$ , this formula can be directly plugged into the basis-functions and OdeBlocks to create a continuous-in-depth transformer, illustrated in Figure 1. Note that the OdeBlock is continuous along the *depth* of the computation; the sequence still uses discrete tokens and positional embeddings. With a forward Euler integrator,  $\Delta t = 1$ , a piecewise constant basis, and  $K = N_T$ , Eq. (17) generates an algebraically equivalent graph to the discrete transformer.

We apply the encoder model to a part-of-speech tagging task, using the English-GUM treebank [47] from the Universal Dependencies treebanks [36]. Our model uses an embedding size of 128, with Key/Query/Value and MLP dimensions of 128 with a single attention head. The final OdeBlock has  $K = 64$  piecewise constant basis functions and takes  $N_T = 64$  steps.

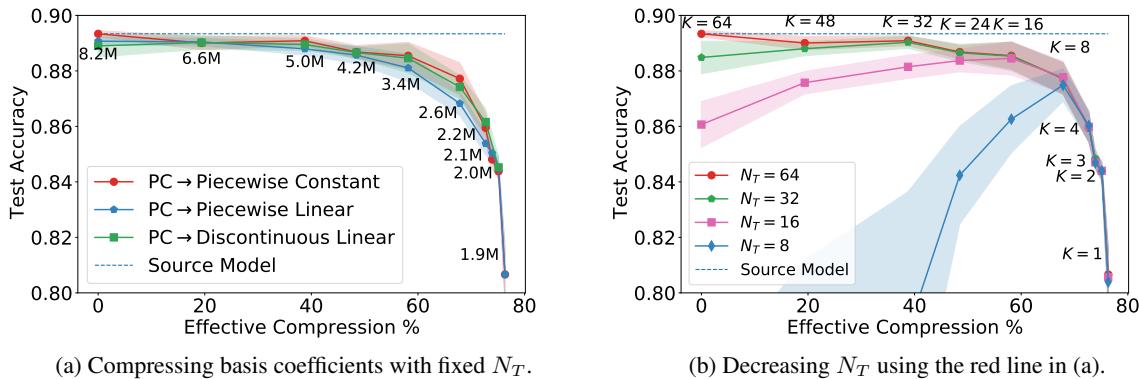


Figure 5: In (a) we show the accuracy of a transformer on a part-of-speech tagging problem as a function of weight compression. The transformer model can be compressed by a factor of 2, while nearly maintaining its predictive accuracy. Discounting the 1.8M embedding parameters, the smallest model achieves 98% compression, albeit losing accuracy. In (b) we show models with different number of time steps  $N_t$  (i.e., models with shorter computational graphs).

In Figure 5a, we present the compression performance for different basis sets. Staying on piecewise constant basis functions yields the best performance during testing (red line). The performance slightly drops when we project the piecewise constant basis onto a piecewise linear basis (blue line). Projecting to a discontinuous linear basis (green line) performs approximately as well as the piecewise constant basis. In Figure 5b, we show the effect of decreasing the number of time steps  $N_T$  during inference time on the predictive accuracy. In the regime where  $N_T \leq K$ , there is no significant loss obtained by reducing  $K$ . Note that there is a divergence when  $N_T > K$ , where the integration method will skip over parameters. However, projection to  $N_T \leq K$  incorporates information across a larger depth-window. Thus, projection improves graph shortening as compared to previous ODE-Nets.

## 8 Conclusion

We introduced a Stateful ODE-based model that can be compressed without retraining, and which can thus quickly and seamlessly be adopted to different computational environments. This is achieved by formulating the weight function of our model as linear combinations of basis functions, which in turn allows us to take advantage of parameter transformations. In addition, this formulation also allows us to implement meaningful stateful normalization layers that are crucial for achieving predictive accuracy comparable to ResNets. Indeed, our experiments showcase that Stateful ODE-Nets outperform other recently proposed ODE-Nets, achieving 94.1% accuracy on CIFAR-10.

When using the multi-level refinement training scheme in combination with piecewise linear basis functions, we are able to compress nearly 50% of the parameters while sacrificing only a small amount of accuracy. On a natural language modeling task, we are able to compress nearly 98% of the parameters, while still achieving good predictive accuracy. Building upon the theoretical underpinnings of numerical analysis, we demonstrate that our compression method reliably generates consistent models without requiring retraining and *without needing to revisit any data*. However, a limitation of our approach is that the implicit regularization effect introduced by the multi-level refinement training scheme can potentially reduce the accuracy of the source model.

Hence, future work should investigate improved training strategies, and explore alternative basis function sets to further improve the compression performance. We can also explore smarter strategies for compression and computational graph shortening by pursuing *hp*-adaptivity algorithms [38]. Further, it is interesting to explore the interplay of our methods with other compression techniques such as sparsification or quantization techniques.

## Acknowledgments

We are grateful for the generous support from Amazon AWS and Google Cloud. NBE and MWM would like to acknowledge IARPA (contract W911NF20C0035), NSF, and ONR for providing partial support of this work. Our conclusions do not necessarily reflect the position or the policy of our sponsors, and no official endorsement should be inferred.

## References

- [1] S. Bai, J. Z. Kolter, and V. Koltun. Deep equilibrium models. In *Advances in Neural Information Processing Systems*, pages 690–701, 2019.
- [2] E. Borges Völker, M. Wendt, F. Hennig, and A. Köhn. HDT-UD: A very large Universal Dependencies treebank for German. *Workshop on Universal Dependencies*, pages 46–57, 2019.
- [3] J. Bradbury, R. Frostig, P. Hawkins, M. J. Johnson, C. Leary, D. Maclaurin, G. Necula, A. Paszke, J. VanderPlas, S. Wanderman-Milne, and Q. Zhang. JAX: composable transformations of Python+NumPy programs, 2018.
- [4] B. Chang, M. Chen, E. Haber, and E. H. Chi. AntisymmetricRNN: A dynamical system view on recurrent neural networks. In *International Conference on Learning Representations*, 2019.
- [5] B. Chang, L. Meng, E. Haber, L. Ruthotto, D. Begert, and E. Holtham. Reversible architectures for arbitrarily deep residual neural networks. In *Proceedings of the AAAI Conference on Artificial Intelligence*, 2018.
- [6] B. Chang, L. Meng, E. Haber, F. Tung, and D. Begert. Multi-level residual networks from dynamical systems view. In *International Conference on Learning Representations*, 2018.
- [7] T. Q. Chen, Y. Rubanova, J. Bettencourt, and D. K. Duvenaud. Neural ordinary differential equations. In *Advances in Neural Information Processing Systems*, pages 6571–6583, 2018.
- [8] M. Cranmer, S. Greydanus, S. Hoyer, P. Battaglia, D. Spergel, and S. Ho. Lagrangian neural networks. In *ICLR 2020 Workshop on Integration of Deep Neural Models and Differential Equations*, 2020.
- [9] E. Dupont, A. Doucet, and Y. W. Teh. Augmented neural odes. In *Advances in Neural Information Processing Systems*, pages 3134–3144, 2019.
- [10] M. Elbayad, J. Gu, E. Grave, and M. Auli. Depth-adaptive transformer. In *International Conference on Learning Representations*, 2020.
- [11] N. B. Erichson, O. Azencot, A. Queiruga, and M. W. Mahoney. Lipschitz recurrent neural networks. *arXiv preprint arXiv:2006.12070*, 2020.
- [12] A. Fan, E. Grave, and A. Joulin. Reducing transformer depth on demand with structured dropout. In *International Conference on Learning Representations*, 2020.
- [13] A. Gholami, K. Keutzer, and G. Biros. ANODE: unconditionally accurate memory-efficient gradients for neural ODEs. In *Proceedings of the AAAI Conference on Artificial Intelligence*, pages 730–736, 2019.
- [14] W. Grathwohl, R. T. Chen, J. Bettencourt, I. Sutskever, and D. Duvenaud. FFJORD: Free-form continuous dynamics for scalable reversible generative models. *arXiv preprint arXiv:1810.01367*, 2018.
- [15] S. Greydanus, M. Dzamba, and J. Yosinski. Hamiltonian neural networks. In *Advances in Neural Information Processing Systems*, pages 15353–15363, 2019.
- [16] J. Gusak, L. Markeeva, T. Daulbaev, A. Katrutsa, A. Cichocki, and I. Oseledets. Towards understanding normalization in neural ODEs. In *ICLR 2020 Workshop on Integration of Deep Neural Models and Differential Equations*, 2020.
- [17] E. Haber and L. Ruthotto. Stable architectures for deep neural networks. *Inverse Problems*, 34(1):014004, 2017.
- [18] E. Hairer, S. P. Nørsett, and G. Wanner. *Solving ordinary differential equations. I. Nonstiff problems*. Springer-Verlag, 1993.
- [19] K. He, X. Zhang, S. Ren, and J. Sun. Deep residual learning for image recognition. In *Proceedings of the Conference on Computer Vision and Pattern Recognition*, pages 770–778, 2016.
- [20] J. Heek, A. Levskaya, A. Oliver, M. Ritter, B. Rondepierre, A. Steiner, and M. van Zee. Flax: A neural network library and ecosystem for JAX, 2020.
- [21] G. Huang, Y. Sun, Z. Liu, D. Sedra, and K. Q. Weinberger. Deep networks with stochastic depth. In *Proceedings of the European Conference on Computer Vision*, pages 646–661. Springer, 2016.
- [22] S. Ioffe and C. Szegedy. Batch normalization: Accelerating deep network training by reducing internal covariate shift. In *International conference on machine learning*, pages 448–456, 2015.
- [23] C. Jordan and K. Jordán. *Calculus of finite differences*, volume 33. American Mathematical Soc., 1965.
- [24] A. Krizhevsky and G. Hinton. Learning multiple layers of features from tiny images. 2009.
- [25] J. Kukacka, V. Golkov, and D. Cremers. Regularization for deep learning: A taxonomy. Technical Report Preprint: arXiv:1710.10686, 2017.
- [26] M. K. Kwong and A. Zettl. *Norm inequalities for derivatives and differences*. Springer, 2006.
- [27] Y. LeCun, L. Bottou, Y. Bengio, and P. Haffner. Gradient-based learning applied to document recognition. *Proceedings of the IEEE*, 86(11):2278–2324, 1998.
- [28] X. Li, A. Cooper Stickland, Y. Tang, and X. Kong. Deep transformers with latent depth. *Advances in Neural Information Processing Systems*, 33, 2020.
- [29] S. H. Lim. Understanding recurrent neural networks using nonequilibrium response theory. *arXiv preprint arXiv:2006.11052*, 2020.
- [30] S. H. Lim, N. B. Erichson, L. Hodgkinson, and M. W. Mahoney. Noisy recurrent neural networks. *arXiv preprint arXiv:2102.04877*, 2021.

- [31] Y. Lu, A. Zhong, Q. Li, and B. Dong. Beyond finite layer neural networks: Bridging deep architectures and numerical differential equations. In *International Conference on Machine Learning*, pages 5181–5190, 2018.
- [32] Y. Lu, A. Zhong, Q. Li, and B. Dong. Beyond finite layer neural networks: Bridging deep architectures and numerical differential equations. In *International Conference on Machine Learning*, pages 3276–3285. PMLR, 2018.
- [33] M. W. Mahoney. Approximate computation and implicit regularization for very large-scale data analysis. In *ACM Symposium on Principles of Database Systems*, pages 143–154, 2012.
- [34] S. Massaroli, M. Poli, J. Park, A. Yamashita, and H. Asma. Dissecting neural odes. In *Advances in Neural Information Processing Systems*, 2020.
- [35] B. Neyshabur. Implicit regularization in deep learning. Technical Report Preprint: arXiv:1709.01953, 2017.
- [36] J. Nivre, M.-C. de Marneffe, F. Ginter, J. Hajič, C. D. Manning, S. Pyysalo, S. Schuster, F. Tyers, and D. Zeman. Universal dependencies v2: An evergrowing multilingual treebank collection. *arXiv preprint arXiv:2004.10643*, 2020.
- [37] A. F. Queiruga, N. B. Erichson, D. Taylor, and M. W. Mahoney. Continuous-in-depth neural networks. *arXiv preprint arXiv:2008.02389*, 2020.
- [38] W. Rachowicz, D. Pardo, and L. Demkowicz. Fully automatic  $hp$ -adaptivity in three dimensions. *Computer methods in applied mechanics and engineering*, 195(37-40):4816–4842, 2006.
- [39] Y. Rubanova, R. T. Chen, and D. Duvenaud. Latent ODEs for irregularly-sampled time series. In *International Conference on Neural Information Processing Systems*, pages 5320–5330, 2019.
- [40] T. K. Rusch and S. Mishra. Coupled oscillatory recurrent neural network (coRNN): An accurate and (gradient) stable architecture for learning long time dependencies. In *International Conference on Learning Representations*, 2021.
- [41] T. K. Rusch and S. Mishra. Unicornn: A recurrent model for learning very long time dependencies. *arXiv preprint arXiv:2103.05487*, 2021.
- [42] L. Ruthotto and E. Haber. Deep neural networks motivated by partial differential equations. *Journal of Mathematical Imaging and Vision*, pages 1–13, 2019.
- [43] E. Weinan. A proposal on machine learning via dynamical systems. *Communications in Mathematics and Statistics*, 5(1):1–11, 2017.
- [44] P. Wriggers. *Nonlinear finite element methods*. Springer Science & Business Media, 2008.
- [45] W. Xu, R. T. Chen, X. Li, and D. Duvenaud. Infinitely deep bayesian neural networks with stochastic differential equations. *arXiv preprint arXiv:2102.06559*, 2021.
- [46] S. Zagoruyko and N. Komodakis. Wide residual networks. *arXiv preprint arXiv:1605.07146*, 2016.
- [47] A. Zeldes. The GUM corpus: Creating multilayer resources in the classroom. *Language Resources and Evaluation*, 51(3):581–612, 2017.
- [48] T. Zhang, Z. Yao, A. Gholami, J. E. Gonzalez, K. Keutzer, M. W. Mahoney, and G. Biros. ANODEV2: A coupled neural ODE framework. In *Advances in Neural Information Processing Systems*, pages 5152–5162, 2019.
- [49] Y. D. Zhong, B. Dey, and A. Chakraborty. Symplectic ODE-Net: Learning Hamiltonian dynamics with control. In *International Conference on Learning Representations*, 2019.
- [50] Q. Zhu, Y. Guo, and W. Lin. Neural delay differential equations. In *International Conference on Learning Representations*, 2021.
- [51] J. Zhuang, N. Dvornik, X. Li, S. Tatikonda, X. Papademetris, and J. Duncan. Adaptive checkpoint adjoint method for gradient estimation in neural ODE. In *International Conference on Machine Learning*, volume 119, pages 11639–11649, 2020.

---

# Stateful ODE-Nets using Basis Function Expansions

## —Supplement Materials—

---

### A Proofs

#### A.1 Proof of Theorem 1

In the sequel, we assert that  $f$  is smooth on an interval  $[0, T]$ , and therefore possesses bounded derivatives of all orders on  $[0, T]$ , where  $T > 0$ . Recall that a  $p$ -stage explicit Runge-Kutta method for an ordinary differential equation  $y'_\theta(t) = f(y_\theta(t), \theta(t))$  provides an approximation  $y_{h,\theta}(t)$  of  $y_\theta(t)$  for a given step size  $h > 0$  through linear interpolation between the recursively generated points:

$$y_{h,\theta}(t+h) = y_{h,\theta}(t) + h\Phi_h(t, y_{h,\theta}(t)),$$

where  $\Phi_h(t, y) = \sum_{i=1}^p b_i k_i(t, y)$  and each

$$k_i(t, y) = f\left(y + h \sum_{j=1}^{i-1} a_{ij} k_j(t, y), \theta(t + c_i h)\right).$$

It is typical to assume that  $c_i = \sum_{j=1}^{i-1} a_{ij}$ . For a fixed Runge-Kutta scheme  $(a_{ij}, b_i, c)$ , let  $I_T$  denote the collection of time points where the scheme evaluates  $\theta(t)$  on the interval  $[0, T]$ , that is,

$$I_T := [0, T] \cap \bigcup_{k \in \mathbb{Z}} \bigcup_{i=1}^p \{kh + c_i h\}.$$

For now, we let  $\bar{\theta}(t)$  denote an arbitrary smooth function satisfying  $\theta(t_j) = \bar{\theta}(t_j)$  for each  $t_j \in I_T$ . This ensures that the Runge-Kutta approximations  $y_{h,\theta}$  and  $\bar{y}_{h,\theta}$  to the ordinary differential equations

$$\begin{aligned} y'_\theta(t) &= f(y_\theta(t), \theta(t)) \\ \bar{y}'_\theta(t) &= f(\bar{y}_\theta(t), \bar{\theta}(t)), \end{aligned}$$

respectively, will coincide (that is,  $y_{h,\theta} = \bar{y}_{h,\theta}$ ). For example, one could take  $\bar{\theta}$  to be the smoothing spline satisfying

$$\bar{\theta}(t) = \arg \min_{\bar{\theta}} \left( \sum_j (\theta(t_j) - \bar{\theta}(t_j))^2 + \int_0^T \|\bar{\theta}^{(p+1)}(t)\| dt \right).$$

Letting

$$\mathcal{D}_\theta^p(t) = \left\{ \frac{\partial^{m+l} f_j}{\partial y^m \partial t^l}(\bar{y}_\theta(t), \bar{\theta}(t)) \right\}_{j=1, \dots, d, k+l \leq p+1},$$

Theorem II.3.2 of [18] implies the existence of a polynomial  $P$  such that for any  $t \in [0, T-h]$ ,

$$\bar{y}_\theta(t+h) = \bar{y}_\theta(t) + h\Phi_h(t, \bar{y}_\theta(t)) + h^{p+1}P \circ \mathcal{D}_\theta^p(t) + \mathcal{O}(h^{p+2}).$$

From [18, Theorem II.3.4], we have also that  $y_{h,\theta}(t) = \bar{y}_\theta(t) + \mathcal{O}(h^p)$ . Furthermore, by [23, §67], for any integer  $m \geq 1$ ,

$$h^{-m} \Delta_h^m f(y, t) = \frac{\partial^m}{\partial t^m} f(y, t) + \mathcal{O}(h),$$

as  $h \rightarrow 0^+$ . Therefore, letting

$$\bar{\mathcal{D}}_{h,\theta}^p(t) = \left\{ h^{-l} \frac{\partial^{m+l}}{\partial y^m} \Delta_h^l(y_{h,\theta}(t), \bar{\theta}(t)) \right\}_{j=1, \dots, d, k+l \leq p+1},$$

we infer that  $\bar{\mathcal{D}}_{h,\theta}^p(t) - \mathcal{D}_\theta^p(t) = \mathcal{O}(h^p) + \mathcal{O}(h) = \mathcal{O}(h)$ . Consequently, for any  $t \in [0, T-h]$ ,

$$\bar{y}_\theta(t+h) = \bar{y}_\theta(t) + h\Phi_h(t, \bar{y}_\theta(t)) + h^{p+1}P \circ \bar{\mathcal{D}}_{h,\theta}^p(t) + \mathcal{O}(h^{p+2}).$$

Moving to a global estimate, [18, Theorem II.8.1] implies that for  $\bar{e}_{h,\theta}(t)$  satisfying

$$\bar{e}'_{h,\theta}(t) = \frac{\partial f}{\partial y}(\bar{y}_\theta(t), \bar{\theta}(t))\bar{e}_{h,\theta}(t) + P \circ \bar{\mathcal{D}}_{h,\theta}^p(t),$$

there is, for any  $t \in [0, T]$ ,

$$y_{h,\theta}(t) = \bar{y}_\theta(t) + h^p \bar{e}_{h,\theta}(t) + \mathcal{O}(h^{p+1}).$$

For any  $t \in [0, T]$ , we let  $\iota_h(t) = \lfloor t/h \rfloor \cdot h$  denote the nearest point on the grid  $\{0, h, 2h, \dots\}$  to  $t$ . Since  $\bar{\theta}$  is Lipschitz continuous on  $[0, T]$ ,  $\theta(\iota_h(t)) = \bar{\theta}(\iota_h(t)) = \bar{\theta}(t) + \mathcal{O}(h)$ . Therefore, by letting

$$\mathcal{D}_{h,\theta}^p(t) = \left\{ h^{-l} \frac{\partial^{m+l}}{\partial y^m} \Delta_h^l(y_{h,\theta}(t), \theta(\iota_h(t))) \right\}_{j=1, \dots, d, k+l \leq p+1},$$

we note that  $\mathcal{D}_{h,\theta}^p(t) = \bar{\mathcal{D}}_{h,\theta}^p(t) + \mathcal{O}(h)$ . Similarly, letting

$$e'_{h,\theta}(t) = \frac{\partial f}{\partial y}(\bar{y}_\theta(t), \theta(\iota_h(t)))e_{h,\theta}(t) + P \circ \mathcal{D}_{h,\theta}^p(t),$$

an application of Gronwall's inequality reveals that  $\bar{e}_{h,\theta}(t) = e_{h,\theta}(t) + \mathcal{O}(h)$ . Therefore,

$$y_{h,\theta}(t) = \bar{y}_\theta(t) + h^p e_{h,\theta}(t) + \mathcal{O}(h^{p+1}).$$

A Taylor expansion in  $L$  finally reveals

$$L(y_{h,\theta}(t)) = L(\bar{y}_\theta(t)) + h^p \nabla L(\bar{y}_\theta(t)) \cdot e_{h,\theta}(t) + \mathcal{O}(h^{p+1}),$$

and hence the result.

## A.2 Proof of Lemma 1

Following the notation used in the proof of Theorem 1, the order conditions for a  $p$ -stage Runge–Kutta method ensure the existence of a function  $\mathcal{E}_{h,\theta}(t)$  uniformly bounded in  $h$  and depending smoothly on  $\theta$ , such that for any  $t \in [0, T]$

$$y_{h,\theta+\epsilon\varphi}(t) = y_{\bar{\theta}+\epsilon\varphi}(t) + h^p \mathcal{E}_{h,\theta+\epsilon\varphi}(t).$$

For more details, see [18, Chapter II.3]. Therefore, as  $h \rightarrow 0^+$ , for any  $t \in [0, T]$ ,

$$D_\varphi y_{h,\theta}(t) = D_\varphi \bar{y}_\theta(t) + \mathcal{O}(h^p).$$

The remainder of the proof follows by straightforward calculation. Since

$$\frac{d}{d\epsilon} \dot{y}_{\bar{\theta}+\epsilon\varphi}(t) = \frac{\partial f}{\partial y}(y_{\bar{\theta}+\epsilon\varphi}(t), \bar{\theta}(t) + \epsilon\varphi(t)) \frac{d}{d\epsilon} y_{\bar{\theta}+\epsilon\varphi}(t) + \frac{\partial f}{\partial \theta}(y_{\bar{\theta}+\epsilon\varphi}(t), \bar{\theta}(t) + \epsilon\varphi(t)) \varphi(t),$$

it follows that

$$\frac{d}{dt} D_\varphi \bar{y}_\theta(t) = \frac{\partial f}{\partial y}(\bar{y}_\theta(t), \bar{\theta}(t)) D_\varphi \bar{y}_\theta(t) + \frac{\partial f}{\partial \theta}(\bar{y}_\theta(t), \bar{\theta}(t)) \varphi(t).$$

Since  $D_\varphi \bar{y}_\theta(0) = 0$ , solving this ODE reveals

$$D_\varphi \bar{y}_\theta(t) = \int_0^t e^{F_\theta(s,t)} \frac{\partial f}{\partial \theta}(\bar{y}_\theta(s), \bar{\theta}(s)) \varphi(s) ds,$$

where  $F_\theta(s,t) = \int_s^t \frac{\partial f}{\partial y}(\bar{y}_\theta(u), \bar{\theta}(u)) du$ . The result now follows since  $y_{h,\theta}(t) = \bar{y}_\theta(t) + \mathcal{O}(h^p)$ , which in turn, implies  $F_{h,\theta} = F_\theta + \mathcal{O}(h^p)$ .

## B Relationships Between Basis Functions and Prior ODE-Nets

The basis function representation of weights provides a systematic way to increase the depth-wise capacity within a single ODE-Net while using the same network unit. Using a single OdeBlock for depth is required for model transformations, such as compression, multi-level refinement, and graph shortening, to make significant changes to the model. In this section, we briefly describe how previous attempts of adding more depth to ODE-Nets with ad hoc changes to the network can be interpreted as basis functions.

For ODE-Nets, the module inside of the time integral is a neural network with time as an additional input:

$$y = \int_0^T F(x, t; \hat{\theta}) dt. \quad (18)$$

Some ODE-Net implementations use  $F(x, t; \hat{\theta}) = \mathcal{R}(x; \hat{\theta})$  with no explicit time dependence [13], which is as if there is a single constant basis function,  $\phi(t) = 1$ . Increasing the number of parameters requires stacking OdeBlocks, which is similar to adding more piecewise constant basis functions [34]. However, and importantly for us, separate OdeBlocks does not allow for integration steps to cross parameter boundaries, and does not enable compression or multi-level refinement.

In other works, e.g., [14], the time dependence is included by appending  $t$  as a feature to the initial input and/or every internal layer of  $\mathcal{R}$  to every other layer as well. In one perspective, this changes the structure of the recurrent unit. However, by algebraic manipulation of  $t$ , we can show that it is similar to a basis function representation plugged into the original recurrent unit,  $\mathcal{R}(x; \theta(t, \hat{\theta}))$ . Suppose the original  $\mathcal{R}$  has two hidden features  $x_1, x_2$ , and six weights  $W_{11}, W_{12}, W_{21}, W_{22}, b_1, b_2$ . In matrix notation, concatenation of  $t$  means that every linear transformation layer (in the  $2 \times 2$  example) has two more weights and can be written as

$$y = \begin{bmatrix} W_{11} & W_{12} & W_{13} \\ W_{21} & W_{22} & W_{23} \end{bmatrix} \begin{Bmatrix} x_1 \\ x_2 \\ t \end{Bmatrix} + \begin{Bmatrix} b_1 \\ b_2 \end{Bmatrix} = \begin{bmatrix} W_{11} & W_{12} \\ W_{21} & W_{22} \end{bmatrix} \begin{Bmatrix} x_1 \\ x_2 \end{Bmatrix} + \begin{Bmatrix} b_1 + W_{13}t \\ b_2 + W_{23}t \end{Bmatrix}.$$

We can rename the third column of  $W$  to be an additional basis coefficient of  $b$ . In tensor notation, we have effectively a representation where one of the weights is based on a simple linear function,

$$y = Wx + b(t),$$

where  $W(t) = W$  is constant in time, but  $b(t) = b + b_t t$ . (This requires mixing basis functions for different components of  $\theta$ ; in the main text, we only used representations where every weight used the same basis.) Thus, this unit is still similar to the original  $\mathcal{R}$ , but only adds another set of bias parameters as a standard ResNet unit.

As an easy extension of the above model, it is also possible to make  $W$  into a linear function of  $t$ ,

$$W(t) = W + W_t t.$$

Then, every component can be included in a parameter function  $\theta(t) = \hat{\theta}_0 + \hat{\theta}_1$ , where every component of the weight parameters is using the same basis set,

$$\begin{aligned} \phi_1(t) &= 1, \\ \phi_2(t) &= t. \end{aligned}$$

These are the first two terms of a polynomial basis set which generalizes as  $\phi_n(t) = t^n$ . The Galerkin ODE-Nets of [34] used general polynomial terms as one basis choice.

Note that the coefficients  $\hat{\theta}_1$  and  $\hat{\theta}_2$  have different ‘‘units’’: ‘‘thetas’’ versus ‘‘thetas-per-second’’. Thus, the weight parameters for the time-coefficients need different initialization schemes, and potentially learning rates, as the weight parameters that are constant-coefficients. To the contrary, the piecewise-constant, piecewise-linear and discontinuous piecewise-linear functions we considered in the main text have basis function coefficients with the same ‘‘units,’’ which can all use standard initialization schemes with no special consideration.

## C Algorithm Details

### C.1 Projection

Numerical integration of the loss function equation is easy to implement, and can be exactly correct for functions with finite polynomial order with sufficient quadrature terms. We break down the domain into sub-cells and use Gaussian quadrature rules on each sub-cell. We use sub-cells because our basis sets are not smooth across control point boundaries. Specifically, we choose  $N_{cell}$  as  $\max(K_1, K_2)$  to line up with the finer partition, where  $K$  denotes the number of basis functions. Further, we use degree 7 quadrature rules.

Given a quadrature rule with  $N_{quad}$  weights  $w_j$  at point  $\xi_j$ , we approximate the projection integral as

$$\int_0^1 f(t) dt \approx \sum_{i=1}^{N_{cell}} \sum_{j=1}^{N_{quad}} w_j f(t_j) \frac{t_{i+1} - t_i}{2}, \quad (19)$$

where  $t_j$  is the mapping of quadrature point  $\xi_j$  from the quadrature domain  $[-1, 1]$  to the cell domain  $[t_i, t_{i+1}]$ . This step is not performance critical, and the summations can be simplified using constant folding at compile time. The operator results in a  $K_1 \times K_2$  matrix that can be applied to every parameter independently.

Now, we describe how to solve the following problem given in the main text:

$$\min_{\hat{\theta}_k^2} \int_0^T \left( \theta^1(t, \hat{\theta}^1) - \theta^2(t, \hat{\theta}^2) \right)^2 dt = \min_{\hat{\theta}_k^2} \int_0^T \left( \sum_{a=1}^{K_1} \hat{\theta}_a^1 \phi_a^1(t) - \sum_{k=1}^{K_2} \hat{\theta}_k^2 \phi_k^2(t) \right)^2 dt. \quad (20)$$

The projection algorithm is applied to each scalar weight of  $\theta$  independently. Let  $X_a$  be one scalar component of  $\hat{\theta}_a^1$  ( $a = 1, \dots, K_1$ ), and  $Y_k$  be the matching scalar component of  $\hat{\theta}_k^2$  ( $k = 1, \dots, K_2$ ). The loss function is defined on the basis coefficients of each scalar weight as

$$L(X, Y) = \sum_{i=1}^{N_{cell}} \sum_{j=1}^{N_{quad}} \frac{w_j(t_{i+1} - t_i)}{2} \left( \sum_{a=1}^{K_1} X_a \phi_a^1(t) - \sum_{k=1}^{K_2} Y_k \phi_k^2(t) \right)^2. \quad (21)$$

This function is quadratic and can be solved with one linear solve,  $Y = -H^{-1}G(x)$  with

$$H_{jk} = \frac{\partial^2 L}{\partial \hat{\theta}^2} = \text{Integrate} \left( \phi_j^2(t) \phi_k^2(t) \right) \quad (22)$$

$$G_j(X) = \frac{\partial L}{\partial \hat{\theta}} = \text{Integrate} \left( \phi_j^2(t) \sum_{a=1}^{K_1} \phi_a^1(t) X_a \right), \quad (23)$$

where  $H$  is a  $K_2 \times K_2$  Hessian matrix, and  $G(X)$  is a  $K_2$  gradient vector. (In practice, we merely implement  $L(X, Y)$  in Python, using NumPy to obtain the quadrature weights, and use JAX's automatic differentiation to evaluate the Hessian  $H$  and gradient  $G$ .) The set of basis function coefficients  $\hat{\theta}^1$  has  $K_1 \times N_{\mathcal{R}}$  components, and  $\hat{\theta}^2$  has  $K_2 \times N_{\mathcal{R}}$  components. This linear solve is applied to every tensor component of  $\hat{\theta}$ , in a loop needing  $N_{\mathcal{R}}$  iterations where  $X$  is a different component of  $\hat{\theta}^1$ . Note that  $H$  is independent of  $X$ , and  $G(X)$  is linear in  $X$  and can be written as  $G(X) = RX$ , where  $R$  is a  $K_2 \times K_1$  matrix. The loop can be efficiently carried out by pre-factorizing  $H$  once, then applying the back-substitution to each column of the the matrix  $R$  to obtain a matrix  $A = H^{-1}R$ . Then,  $A$  can be applied to every component column in  $\hat{\theta}^1$ , obtaining a linear operation

$$\underbrace{[\hat{\theta}^2]}_{K_2 \times N_{\mathcal{R}}} = - \underbrace{[H^{-1}]}_{K_2 \times K_2} \underbrace{[G]}_{K_2 \times K_1} \underbrace{[\hat{\theta}^1]}_{K_1 \times N_{\mathcal{R}}}. \quad (24)$$

Projection of the updated state point cloud onto the basis in Equation (13) can be solved with the same algorithm by letting  $L(X, Y)$  equal to the minimization objection. Gaussian quadrature is not needed to calculate  $L$ , and automatic differentiation can be directly applied to the least-squares summation over the point cloud.

**A Note on Complexity.** Basis transformations are data agnostic, i.e., they operate directly on the parameter coefficients. The total number of parameters for the two basis function models is  $N_{\mathcal{R}}K_1$  and  $N_{\mathcal{R}}K_2$ , where  $N_{\mathcal{R}}$  is the number of coordinates of  $\mathcal{R}$ . Projection requires one matrix factorization and  $N_{\mathcal{R}}$  applications of the factorization; the general-case complexity is  $\mathcal{O}((K_2)^3 + (K_2)^2K_1 + N_{\mathcal{R}}K_1K_2)$ . Interpolation requires  $K_2$  evaluations of  $\phi^1$  for each coordinate; the general-case complexity of interpolation is  $\mathcal{O}(N_{\mathcal{R}}K_2K_1)$ .  $K_1$  and  $K_2$  are proportional to the number of layers in a model and thus relatively small numbers, as compared to  $N_{\mathcal{R}}$ .

## C.2 Stateful Normalization Layer

Algorithm 1 lists the forward pass during training. Tracking a list of updated module states (i.e. BatchNorm statistics) at times  $t_i$  is fused with integrating the ODE-Net forwards in time. By using a fixed times integration scheme (with constant  $\Delta t$ ), this algorithm yields a static computational graph. In practice, by using basis functions with compact support, the computational graph can further optimized by interleaving the Project calculation with the integration loop. At inference time, the state parameters are fixed, so it is not necessary to compute  $\mathcal{R}_s$ , save the list States, or perform projection to  $\hat{\theta}^{s*}$ .



---

**Algorithm 1:** StatefulOdeBlock accumulates and projects state updates from the Runge-Kutta forward pass.

---

**Data:** Gradient and state parameters  $\hat{\theta}^g, \hat{\theta}^s$ , Input  $x_{in}$ .  
Initialize States = {};  
Let  $x = x_{in}$ ;  
**for**  $t = 0, t < T, t = t + \Delta t$  **do**  
    **foreach** *Runge-Kutta Stage i* **do**  
        Let  $t_i = t + c_i \Delta t$ ;  
         $x_i = \sum_j x + \Delta t a_{ij} k_j$ ;  
         $k_i = \mathcal{R}_x(\theta^g(t_i, \hat{\theta}^g), \theta^s(t_i, \hat{\theta}^s), x_i)$ ;  
         $\hat{\theta}_i^s = \mathcal{R}_s(\theta^g(t_i, \hat{\theta}^g), \theta^s(t_i, \hat{\theta}^s), x_i)$ ;  
        States.append( $\{t_i, \hat{\theta}_i^s\}$ );  
    **end**  
    Let  $x = x + \Delta t \sum_i b_i k_i$ ;  
**end**  
 $x_{out} = x$ ;  
 $\hat{\theta}^{s*} = \text{Project}(\text{States}, \phi, K)$ ;  
**Forward pass outputs:**  $x_{out}, \hat{\theta}^{s*}$ ;  
**Use**  $x_{out}$  to compute *loss*.;  
**Backward pass:** Trace  $\partial x_{out} / \partial \hat{\theta}^g$ ;  
**Update gradient parameters:**  $\theta^g \leftarrow \text{OptimizerStep}(\hat{\theta}^g, \partial \text{loss} / \partial \hat{\theta}^g)$ ;  
**Update state parameters:**  $\hat{\theta}^s \leftarrow \hat{\theta}^{s*}$ ;

---

### C.3 Refinement Training

Piecewise constant basis functions yield a simple scheme to make a neural network deeper and increase the number of parameters: double the number of basis functions, and copy the weights to new grid. This insight was used by [6] and [37] to accelerate training. In these prior works, network refinement was implemented by copying and re-scaling discrete network objects, or expanding tensor dimensions.

Instead, we view this problem through the lens of basis function interpolation and projection. The procedure can be thought of as projecting or interpolating to a basis set with more functions:

$$\hat{\theta}^{refined} = \text{Interpolate} \left( \left( \sum_{k=1}^K \hat{\theta}_k \phi_k(t) \right), \text{next}(\phi), \text{next}(K) \right), \quad (25)$$

where  $\text{next}(\cdot)$  is an arbitrary schedule picking the new basis functions.  $\text{Project}$  can also be used instead of  $\text{Interpolate}$ . The multi-level refinement training of [6, 37] is equivalent to interpolating a piecewise constant basis set to twice as many basis functions by evaluating  $\hat{\theta}_k^2 = \theta^1(t_k)$  at new cell centers  $t_k = T(k-1)/(K_2-1)$ . For exactly doubling the number of parameters, the evaluation of  $\sum \hat{\theta}^1 \phi^1(t_k)$  can be simplified as a vector of twice as many basis coefficients,

$$\hat{\theta}^2 = \{\hat{\theta}_1^1, \hat{\theta}_1^1, \hat{\theta}_2^1, \hat{\theta}_2^1 \dots \hat{\theta}_{K_1}^1, \hat{\theta}_{K_1}^1\}, \quad K_2 = 2K_1. \quad (26)$$

The ‘‘splitting’’ concept can be extended to piecewise linear basis functions by adding an additional point into the midpoint of cells. The midpoint control point evaluates to the average of the parameters at the endpoints. This results in the new list of coefficients

$$\hat{\theta}^2 = \left\{ \hat{\theta}_1^1, \frac{\hat{\theta}_1^1 + \hat{\theta}_2^1}{2}, \hat{\theta}_2^1, \frac{\hat{\theta}_2^1 + \hat{\theta}_3^1}{2}, \hat{\theta}_3^1 \dots \hat{\theta}_{K_1-1}^1, \frac{\hat{\theta}_{K_1-1}^1 + \hat{\theta}_{K_1}^1}{2}, \hat{\theta}_{K_1}^1 \right\}, \quad K_2 = 2K_1 - 1. \quad (27)$$

Both of these splitting-based interpolation schemes are exactly correct for piecewise constant and piecewise linear basis functions. Multi-level refinement training can be applied to any basis functions and any pattern for increasing  $K$  by using the general interpolation and projection methods.

Table 5: Compression performance and test accuracy of Deep ODE-Nets on CIFAR-100.

Model	Best	Average	Min	# Parameters	Compression
Wide-ResNet [46]	-	78.8%	-	17.2M	-
ResNet-122-i [6]	-	73.2%	-	7.7M	-
Wide-ContinuousNet [37]	79.7%	78.8%	78.2%	13.6M	-
Stateful ODE-Net (c1)	76.2%	76.9%	75.5%	15.2M	-
↪ (compressed)	75.9%	75.6%	75.2%	9.0M	41%
Stateful ODE-Net (c2)	<b>79.9%</b>	<b>79.1%</b>	<b>78.5%</b>	13.6M	-
↪ (compressed)	52.7%	48.9%	39.5%	9.0M	34%

To make sure that the ODE integration in the forward pass visits all of the new parameters, we also increase the number of steps  $N_T$  after refinement. A sketch of a training regiment using interpolation is shown in Algorithm 2.

---

**Algorithm 2:** Sketch of a training algorithm using multi-level refinement training as an interpolation step. The interpolation step is applied to all of the *StatefulOdeBlocks* inside of the model. The same interpolation is applied to gradient parameters and state parameters. Interpolation can be replaced by projection.

---

```

def next( $K$ ) = Pattern to increase basis functions; e.g.  $\text{next}(K) = 2K$ .;
def loss(model,  $\hat{\theta}^g, \hat{\theta}^s, \text{batch}$ ) = logits( $Y, \text{model}(\hat{\theta}^g, \hat{\theta}^s, X)$ );
model = ContinuousModel( $N_{T, \text{initial}}, \text{scheme}, K_{\text{initial}}, \phi$ );
 $\hat{\theta}^g, \hat{\theta}^s$  = Initialize(model);
Optimizer = MakeOptimizer(loss,  $\hat{\theta}^g$ );
for  $e \in [1, \dots, N_{\text{epochs}}]$  do
  if  $e \in \text{Refinement Epochs}$  then
     $\hat{\theta}^g$  = Interpolate( $\hat{\theta}^g, \phi, \text{next}(\text{model}.K)$ );
     $\hat{\theta}^s$  = Interpolate( $\hat{\theta}^s, \phi, \text{next}(\text{model}.K)$ );
    model. $K$  = next(model. $K$ ) # Update the model hyperparameters to track  $K$ .;
    model. $N_T$  = next(model. $N_t$ ) # Also increase the number of integration steps.;
    Optimizer = MakeOptimizer(loss,  $\hat{\theta}^g$ );
  for batch  $\in$  Training Data do
     $l, \hat{\theta}^s$  = loss(model,  $\hat{\theta}^g, \hat{\theta}^s, \text{batch}$ );
     $\hat{\theta}^g$  = Optimizer( $\hat{\theta}^g, \nabla l$ );
  Save Checkpoint( $\hat{\theta}^g, \hat{\theta}^s$ );

```

---

## D Additional Results

### D.1 Results for CIFAR-100.

Table 5 tabulates results for applying the same methodology to CIFAR-100. Again, we consider two configurations: (c1) is a model trained with refinement training, which has piecewise linear basis functions; (c2) is a model trained without refinement training, which has piecewise constant basis functions. Similar to the results for CIFAR-10, we see that model (c2) achieves high predictive accuracy, however, the compression performance is poor. Our model (c1) is less accurate, but we are able to compress the number of parameters by about 41% with less than 1% loss of accuracy on average.

### D.2 Continuous Transformers Applied to German-HDT

We applied the same architecture as Section 6.3 to the German-HDT dataset as well [2]. This dataset has a vocabulary size of 100k (vs. 19.5k) and 57 labels (vs. 53). All other hyperparameters and learning rate schedule are the same as the original transformer. The final trained source model also has  $K = 64$  basis functions. The compression and graph shortening experiments are repeated for this cohort of models, again sampled from 8 seeds, and the results are shown in Figure 6. We also perform the procedure of projecting the source model with  $K = 64$  down to the smallest possible model,  $K = 1$ . Because of the increased vocabulary size, the embedding table

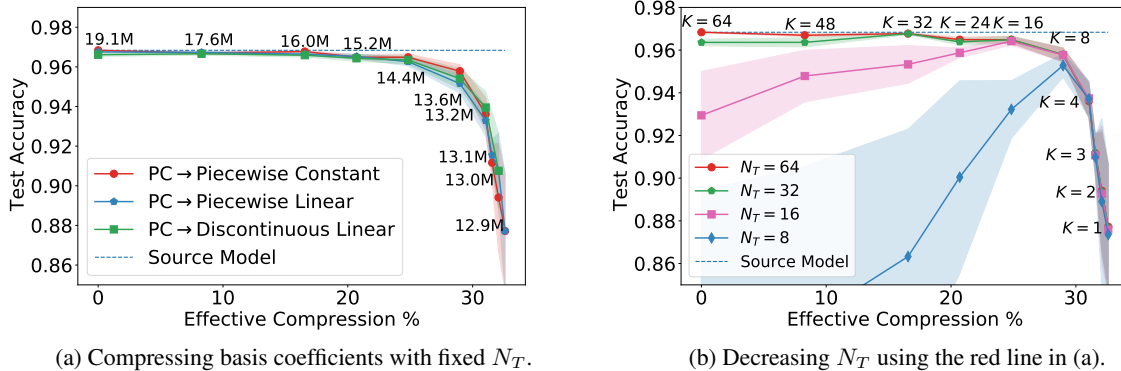


Figure 6: In (a), we show the compression of a continuous-in-depth transformer for part-of-speech tagging. Discounting the 12.8M parameters in the embedding table and only considering the parameters in the transformer layers and classifier, the smallest model ( $K = 1$ ) achieves 98.3% compression compared to the source model ( $K = 64$ ). In (b) it is observed that the model graph can be shortened.

is much larger, and thus the effective compression at  $K = 1$  is only 32%. We observe the same behavior as in the English-GUM dataset. The resulting models are more accurate for this dataset, but the relative performance trade-off with respect to compression is similar.

## E Model Configurations

Here, we present details about the model architectures that we used for our experiments. (The provided software implementation provides further details.)

### E.1 Image Classification Networks

At a high-level, our models are composed of two types of blocks that allow us to construct computational graphs that are similar to those of ResNets.

- The *StatefulOdeBlock* can be regarded as a drop-in replacement for standard ResNet blocks. The ODE rate,  $\mathcal{R}$  takes the form of the residual units. For instance, for image classification tasks, this block consists of two convolutional layers in combination with pre-activations and BatchNorms. Specifically, we use the following structure:

$$\mathcal{R} = x \rightarrow BN \rightarrow ReLU \rightarrow Conv \rightarrow BN \rightarrow ReLU \rightarrow Conv.$$

However, the user can define any other structure that is suitable for a particular task at hand.

- The *StichBlock* has a similar form as compared to the OdeBlock (two convolutional layers in combination with pre-activations), but in addition this block allows us to perform operations such as down-sampling by replacing the skip connection with a stride of 2.

The number of channels and strides can be chosen the same way as for discrete ResNet configurations. In the following we explain the detailed structure of the different models used in our experiments. For simplicity, we omit batch normalization layers and non-linear activations.

**Shallow ODE-Net for MNIST.** Table 6 describes the initial configuration for our MNIST experiments. Here the initial architecture consists of a convolutional layer followed by a *StichBlock* and a *StatefulOdeBlock* with 12 channels. During training we increase the number of basis functions in the *StatefulOdeBlock* from 1 to 8, using the multi-level refinement training scheme.

*Training details.* We train this model for 90 epochs with initial learning rate 0.1 and RK4. We refine the model at epochs 20, 50, and 80. We use batch size 128 and stochastic gradient descent with momentum 0.9 and weight decay of 0.0005 for training.

**Shallow ODE-Net for CIFAR-10.** Table 7 describes the initial configuration for our CIFAR-10 experiments. Here the initial architecture consists of a convolutional layer followed by a *StichBlock* and a *StatefulOdeBlock* with 16

Table 6: Summary of architecture used for MNIST.

Name	output size	Channel In / Out	Kernel Size	Stride	Residual
conv1	28×28	1 / 12	3×3	1	No
StichBlock_1	28×28	12 / 12	$\begin{bmatrix} 3 \times 3 \\ 3 \times 3 \end{bmatrix}$	1	Yes
StatefulOdeBlock_1	28×28	12 / 12	$\begin{bmatrix} 3 \times 3 \\ 3 \times 3 \end{bmatrix}$	-	Yes

Name	Kernel Size	Stride
average pool	8×8	8

Name	input size	output size
FC	-	10

channels, followed by another *StichBlock* and *StatefulOdeBlock* with 32 channels. The second *StichBlock* has stride 2 and performs a down-sampling operation. During training we increase the number of basis functions in both *StatefulOdeBlocks* from 1 to 8, using the multi-level refinement training scheme. That is, each *StatefulOdeBlock* has a separate basis function set, but both have the same  $K$ .

*Training details.* We train this model for 200 epochs with initial learning rate 0.1 and RK4. We refine the model at epochs 50, 110, and 150. We use a batch size of 128 and stochastic gradient descent with momentum 0.9 and weight decay of 0.0005 for training.

Table 7: Summary of shallow architecture used for CIFAR-10.

Name	output size	Channel In / Out	Kernel Size	Stride	Residual
conv1	28×28	3 / 16	3×3	1	No
StichBlock_1	32×32	16 / 16	$\begin{bmatrix} 3 \times 3 \\ 3 \times 3 \end{bmatrix}$	1	Yes
StatefulOdeBlock_1	32×32	16 / 16	$\begin{bmatrix} 3 \times 3 \\ 3 \times 3 \end{bmatrix}$	-	Yes
StichBlock_2	16×16	16 / 32	$\begin{bmatrix} 3 \times 3 \\ 3 \times 3 \end{bmatrix}$	2	Yes
StatefulOdeBlock_2	16×16	32 / 32	$\begin{bmatrix} 3 \times 3 \\ 3 \times 3 \end{bmatrix}$	-	Yes

Name	Kernel Size	Stride
average pool	8×8	8

Name	input size	output size
FC	-	10

**Deep ODE-Net for CIFAR-10.** Table 7 describes the initial configuration for our CIFAR-10 experiments using deep ODE-Nets. Here the initial architecture consists of a convolutional layer followed by a *StichBlock* and a *StatefulOdeBlock* with 16 channels, followed by another *StichBlock* and *StatefulOdeBlock* with 32 channels, followed by another *StichBlock* and *StatefulOdeBlock* with 64 channels. The second and third *StichBlock* have stride 2 and perform down-sampling operations. During training we increase the number of basis functions in each of the three *StatefulOdeBlocks* from 1 to 16, using the multi-level refinement training scheme. The three *StatefulOdeBlock* uniformly have the same number of basis functions.

*Training details.* We train this model for 200 epochs with initial learning rate 0.1 and RK4. We refine the model at epochs 20, 40, 70, and 90. We use batch size 128 and stochastic gradient descent with momentum 0.9 and weight decay of 0.0005 for training.

**Deep ODE-Net for CIFAR-100.** For our CIFAR-100 experiments we use the same initial configuration as for CIFAR-10 in Table 7, with the difference that we increase the number of channels by a factor of 4. Then, during training we increase the number of basis functions in each of the *StatefulOdeBlocks* from 1 to 8, using the multi-level refinement training scheme.

*Training details.* We train this model for 200 epochs with initial learning rate 0.1 and RK4. We refine the model at epochs 40, 70, and 90. We use batch size 128 and stochastic gradient descent with momentum 0.9 for training.

Table 8: Summary of deep shallow architecture used for CIFAR-10.

Name	output size	Channel In / Out	Kernel Size	Stride	Residual
conv1	28×28	3 / 16	3×3	1	No
StichBlock_1	32×32	16 / 16	$\begin{bmatrix} 3 \times 3 \\ 3 \times 3 \end{bmatrix}$	1	Yes
StatefulOdeBlock_1	32×32	16 / 16	$\begin{bmatrix} 3 \times 3 \\ 3 \times 3 \end{bmatrix}$	-	Yes
StichBlock_2	16×16	16 / 32	$\begin{bmatrix} 3 \times 3 \\ 3 \times 3 \end{bmatrix}$	2	Yes
StatefulOdeBlock_2	16×16	32 / 32	$\begin{bmatrix} 3 \times 3 \\ 3 \times 3 \end{bmatrix}$	-	Yes
StichBlock_3	8×8	32 / 64	$\begin{bmatrix} 3 \times 3 \\ 3 \times 3 \end{bmatrix}$	2	Yes
StatefulOdeBlock_3	8×8	64 / 64	$\begin{bmatrix} 3 \times 3 \\ 3 \times 3 \end{bmatrix}$	-	Yes

Name	Kernel Size	Stride
average pool	8×8	8

Name	input size	output size
FC	-	10

## E.2 Part-of-Speech Tagging Networks

For our part-of-speech tagging experiments, we use the continuous transformer illustrated in Figure 1 of the main text. This network only has four major components: the input sequence is fed into an embedding table loop up, then concatenated with a position embedding, and then fed into a single *StatefulOdeBlock*. The output embeddings are used by a fully connected layer to classify each individual token in the sequence. The network structure of the module  $\mathcal{R}$  for the encoder is diagrammed on the right side of Figure 1. Note that the  $dx/dt$  encoder has slightly rearranged skip connections from the discrete encoder. The Self Attention and MLP blocks apply layer normalization to their inputs. In our implementation, we did not use additional dropout layers.

Every vector in the embedding table is of size 128. The kernel dimensions of the query, key, and value kernels of the self attention are 128. The MLP is a shallow network with 128 dimensions.

*Training details.* We train this model for 35000 iterations, with a batch size of 64. We use Adam for training. The learning rate follows an inverse square-root schedule, with an initial value of 0.1 and a linear ramp up over the first 8000 steps. The optimizer parameters are  $\beta_1 = 0.9$ ,  $\beta_2 = 0.98$ , and  $\epsilon = 10^{-9}$ , with weight decay of 0.1. The refinement method is applied at steps 1000, 2000, 3000, 4000, 5000, and 6000 to grow the basis set from  $K = 1$  to  $K = 64$ .